GEOLOGY

Scaling laws for sediment storage and turnover in river floodplains

Emily C. Geyman[1]*, Yutian Ke[1], John S. Magyar[1], Jocelyn N. Reahl[2], Vincent Soldano[3], Nathan D. Brown[4], A. Joshua West[5], Woodward W. Fischer[1], Michael P. Lamb[1]

Nearly 10% of Earth's continents are covered by river floodplains. These landscapes serve as weathering reactors whereby particles eroded from mountains undergo chemical and physical alteration before being exported to oceans. The time a particle spends in floodplain reservoirs regulates the style and extent of continental chemical weathering and the fate of terrestrial organic carbon. Despite its importance for the global carbon cycle, we still lack a quantitative understanding of floodplain storage timescales. Using a combination of geomorphic mapping, radiocarbon and luminescence dating, and numerical simulations of meander dynamics, we identify well-conserved scaling laws that describe floodplain storage times. Our results reveal that, to first order, floodplain storage durations are set by the ratio of river width to migration rate. The fact that most rivers erode about 1% of their width per year leads to a typical floodplain storage duration of ~5 thousand years.

INTRODUCTION

Rivers are the arteries that transfer water, sediment, nutrients, and organic carbon from the continents to ocean basins. In the broad, low-gradient alluvial valleys that cover much of Earth's surface, rivers act not as stationary canals but as dynamic systems that persistently (i) erode alluvial sediment on their outer banks, (ii) deposit sediment on their inner banks, and (iii) transport sediment downstream (Fig. 1A). These river "reactors" set the timescale of sediment persistence on the floodplain, which determines processes such as the aging and degradation of terrestrial organic carbon (*1*–*4*), the style and intensity of continental chemical weathering (*5*–*9*), the persistence and removal of particle-bound contaminants (*10*–*13*), and the degree of buffering and/or shredding of climate signals that get preserved in sedimentary basins (*14*–*16*).

If floodplains were well-mixed reservoirs without net erosion or accretion, one could describe the timescale for sediment turnover with a simple one-box model. For example, consider the control volume of a river floodplain with reach length L, channel depth H, and floodplain width W_f (Fig. 1A). The total volume of sediment in this control reach is $W_f LH$ (L^3). A river traversing this floodplain with average migration rate M_{avg} and sinuosity S has a volumetric reworking rate of $M_{avg}SLH$ ($L^3\ T^{-1}$). Thus, the residence time of sediment in the floodplain, τ, would be

$$\tau = \frac{W_f LH}{M_{avg} SLH} = \frac{W_f}{M_{avg} S} \quad (1)$$

For example, a river with migration rate $M_{avg} = 5$ m/year, sinuosity $S = 1.5$, and floodplain width $W_f = 15$ km would yield $\tau = 2$ thousand years (kyr). However, floodplains cannot adequately be described as uniform, well-mixed reservoirs because their turnover is controlled by the position of the river channel, which exhibits a high degree of autocorrelation across space and time (Fig. 1B) (*4*, *17*, *18*). Previous workers have proposed that, on very long timescales, the position of a meandering channel obeys a sort of "random walk" (*4*, *17*, *19*). This random-walk framing successfully explains how portions of the floodplain near the active channel are repeatedly reworked, whereas pockets of much older terrain can persist on the edges of the alluvial valley, leading to a heavy-tailed distribution of floodplain particle ages (Fig. 1B) (*4*, *17*).

However, a limitation of this conceptualization is that, on short timescales, rivers exhibit a behavior opposite to a random walk; their position is highly deterministic and controlled by the local river curvature (Fig. 1C) (*20*). Two relevant timescales to contextualize this regime of deterministic behavior are (i) the time it takes a channel to erode a distance equivalent to one channel width (τ_w)

$$\tau_w = \frac{W}{M_{avg}} \quad (2)$$

and (ii) the time required for a single meander to evolve to the point of cutoff (τ_{cut}) (*4*, *17*, *18*). At timescales on the order of several τ_w or shorter, meander kinematics dictate that newly deposited inner-bank sediment has high preservation potential because the channel tends to be migrating away from the point of interest (Fig. 1C). In contrast, at timescales approaching τ_{cut}, meander cutoff events abruptly change the position of the channel and cause nearby floodplain sediments to be preferentially eroded, rather than preferentially protected. Thus, previous models (*4*, *17*), which are predicated on the notion that rivers preferentially erode younger deposits (*4*, *17*), only apply for timescales on the order of τ_{cut} or longer.

How long is this cutoff timescale? Using a combination of numerical simulations and an analysis of historical satellite imagery (see the Supplementary Materials), we estimate the cutoff time distribution for three large databases of rivers on Earth (*21*–*23*). Figure 2B shows the resulting distribution of τ_{cut}; the mean cutoff timescale is 3.2 ± 1.8 kyr. Thus, to understand how fluvial systems respond to environmental perturbations on timescales shorter than a few thousand years, which include all anthropogenic perturbations, we need models that apply to timescales shorter than τ_{cut}.

We hypothesize that meander kinematics cause the age distribution of floodplain sediment to be characterized by distinct scaling

[1]Division of Geological and Planetary Sciences, California Institute of Technology, Pasadena, CA 91125, USA. [2]Department of Geological Sciences, University of Colorado, Boulder, CO 80309, USA. [3]Department of Geological Sciences and Engineering, University of Nevada, Reno, NV 89557, USA. [4]Department of Earth and Environmental Sciences, University of Texas, Arlington, TX 76019, USA. [5]Department of Earth Sciences, University of Southern California, Los Angeles, CA 90089, USA.
*Corresponding author. Email: egeyman@caltech.edu

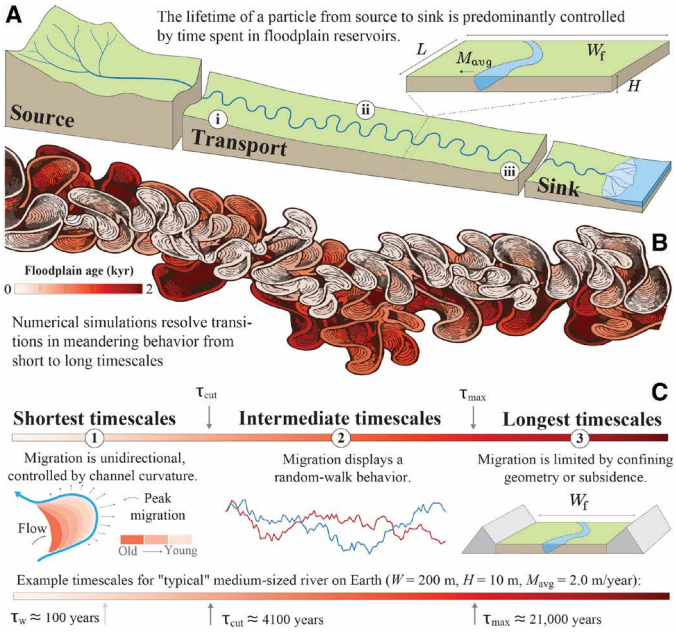

Fig. 1. River meandering on short to long timescales. (**A**) An illustration of the transport of sedimentary particles from an upland source region to a terminal sink. Between the source and the sink, particles often pass through a low-gradient alluvial river system, where they are repeatedly deposited within the floodplain via lateral river migration, then stored for a duration before the river revisits the same location and erodes the particle, and then transported downstream before being deposited again. The duration of each floodplain storage event and the number of storage events control the total transport time from source to sink (*4*). We are interested in quantifying three interrelated quantities: [(A), i] the age distribution of sediment on the floodplain, [(A), ii] the age distribution of eroded sediment (which represents the floodplain storage time distribution), and [(A), iii] the age distribution of sediment transported down the river (where the particles have undergone *n* sequential storage and release events) (*4*). (**B**) Numerical simulations (*4*, *17*, *18*, *29*, *42*, *43*) provide an opportunity to probe the long-timescale behavior of meandering rivers and evaluate the controls on the ages of stored and transported particles. (**C**) We hypothesize that river meandering leads to three types of behavior on short to long timescales: ① On the shortest timescales, river migration follows a predictable pattern governed by the local channel curvature (*20*), and sediment deposited in the inner bend tends to be protected from subsequent erosion because the channel is migrating away from the point of interest. ② At intermediate timescales (e.g., longer than the timescale when a meander bend grows to the point of cutoff, τ_{cut}), the river adopts a random-walk behavior (*4*, *17*). ③ At sufficiently long timescales, the total area visited by the river is limited by factors such as long-term subsidence and aggradation and/or the bounding valley geometry.

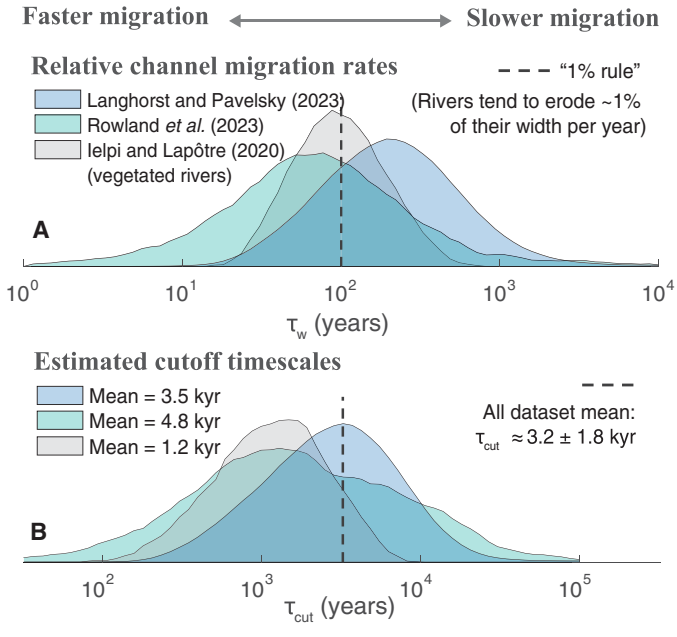

Fig. 2. Estimates of the characteristic timescales τ_w and τ_{cut} for three global datasets of meandering rivers on Earth. The datasets include not only single-threaded meandering but also anabranching and distributary (deltaic) channels. See Supplementary Text for details on how the analysis was performed. (**A**) The characteristic timescale τ_w describes the time it takes for a channel to erode a distance equivalent to one channel width. A τ_w value of 100 years means that the channel erodes 1% of its width per year. Larger τ_w denotes slower relative channel migration. (**B**) The cutoff timescale τ_{cut} depends on τ_w, as well as the channel width-to-depth ratio (fig. S1). Weighting the datasets in (*21*–*23*) equally, the mean estimated τ_{cut} for modern rivers on Earth is approximately 3.2 ± 1.8 kyr.

behavior at three temporal scales (Fig. 1C). At the shortest timescales, there is an "excess" of floodplain sediment because alluvial material is deposited but rarely eroded because it resides in the sheltered wake of a meander (although note that the downstream translation of meander bends tends to clip off a fraction of the newly deposited inner-bank sediment) (*20*, *24*). At intermediate timescales, the channel can be thought of as performing a random walk (*17*, *19*), revisiting different parts of the floodplain in a manner that is approximately diffusive in nature (*17*). Last, because river floodplains are not infinitely wide but rather constrained by bounding topography or else in a state of aggradation, there exists some timescale τ_{max} at which the probability of encountering a pocket of older floodplain sediment falls toward zero (Fig. 1C) (*4*).

Here, we seek quantitative and predictive models that describe the transitions between these three scaling behaviors and span a wide range of timescales from ~10^0 to 10^6 years. It is now routine to quantify characteristics such as river width (*25*) and migration rate (*21*, *26*, *27*) from satellite data. Our motivating question is as follows: Given a set of easily measurable river characteristics—channel width, migration rate, and floodplain width—can we determine a priori the age distribution of the floodplain?

We combine numerical models of river meandering with field observations to test scaling laws. Because there exist very few observations of age-area relationships in alluvial floodplains (i.e., those used to ground-truth simulations similar to the one shown in Fig. 1B) (*28*), we begin by combining geomorphological mapping with geochemical age constraints to produce floodplain age maps for three distinct environments: (i) a gravel-bedded, anastomosing reach; (ii) a sand-bedded, single-threaded meandering reach; and (iii) a sand-to-silt–bedded distributary deltaic system (Fig. 3, A to C). Next, we run numerical meander simulations (*29*) to explore how parameters such as the migration rate, the channel width, and the total floodplain width determine the age distribution of the floodplain. We find that the behavior across all simulations collapses to a simple scaling behavior defined by three power-law regimes (which correspond to the three regimes hypothesized in Fig. 1C). We show how this empirical relation correctly reproduces the age-area relationships at our three field sites (Fig. 3) without tuning, and

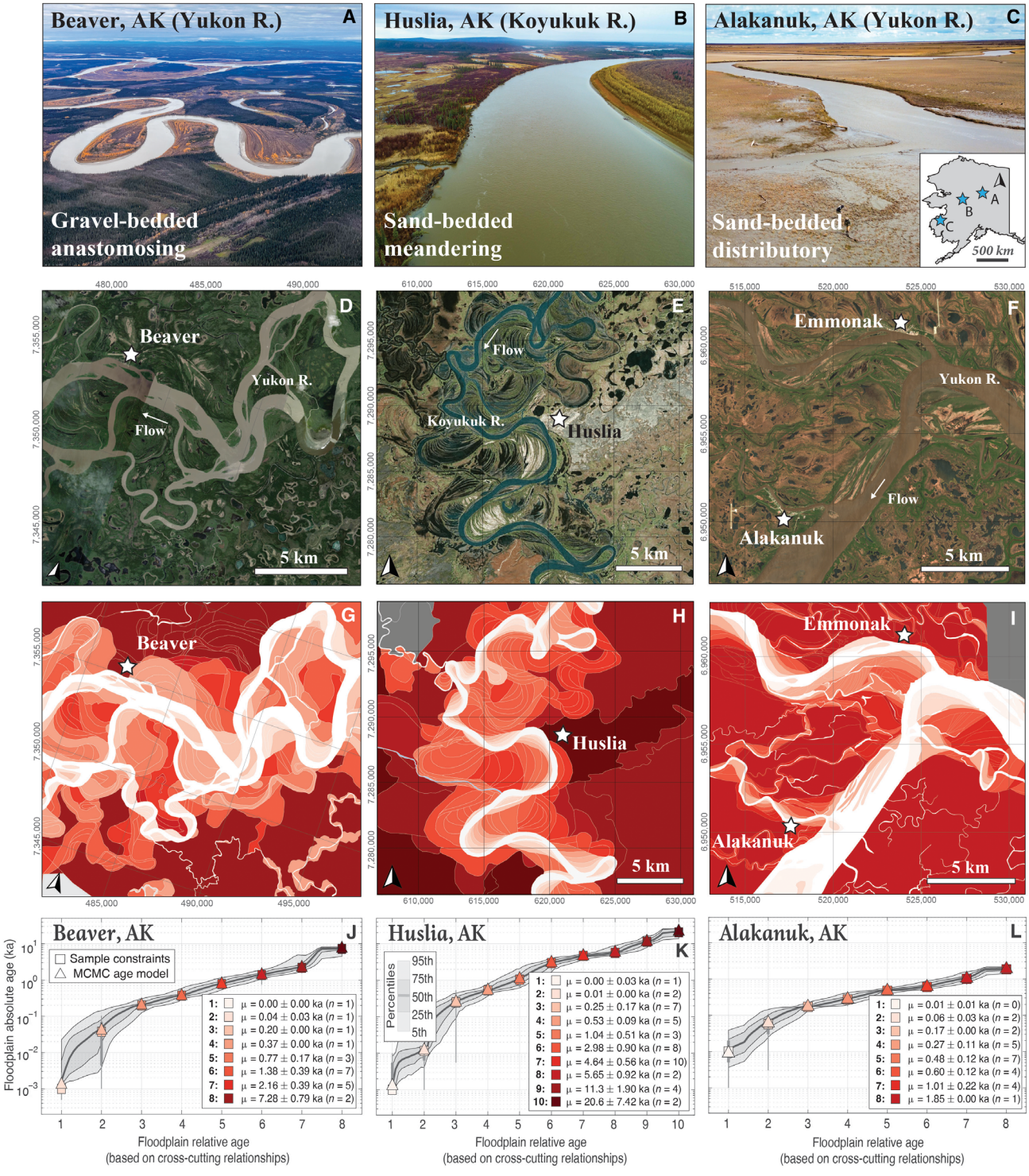

Fig. 3. Field sites where we constrain floodplain age-area relationships. (**A** to **C**) We study three locations with different alluvial river morphologies: (A) the gravel-bedded, anastomosing Yukon River near Beaver, Alaska (66.362°N, 147.398°W); (B) the sand-bedded, single-threaded meandering Koyukuk River near Huslia, Alaska (65.700°N, 156.387°W); and (C) the sand-bedded, tidally influenced channels of the Yukon River Delta near Alakanuk, Alaska (62.685°N, 164.644°W). We use cross-cutting relationships of fluvial deposits observed in satellite imagery (**D** to **F**) to develop an ordinated chronology of the relative floodplain age (**G** to **I**). To convert relative ages to absolute ages, we sampled floodplain material for radiocarbon (^{14}C) and optically stimulated luminescence (OSL) analyses. In (**J**) to (**L**), the squares denote the mean and SD of the *n* geochemical samples collected from each relative age unit. Note that the temporal ordination of the relative age units imposes an additional constraint that we can incorporate into our age model (*33*). Using Markov chain Monte Carlo (MCMC) methods (*33*), we generate estimates for the age and uncertainty of each mapped unit. Image credit for (A) to (C): E.C.G., Caltech.

how it flexibly applies to both single-threaded and anabranching meandering systems.

Field observations of floodplain age-area relationships

At each of the sites shown in Fig. 3, we quantified the age distribution of floodplain sediment through a combination of geomorphic mapping and geochemical sampling (Fig. 3) (*30*). Our methodology involves three steps:

1) Developing relative floodplain age chronologies. Cross-cutting relationships of lateral accretion sets (LASs) encode the relative ages of fluvial deposits (*31*). That is, a deposit must be younger than the deposits that it cross-cuts and older than any deposits that cross-cut it (*30*, *31*). Using this principle, we created floodplain relative age maps, where floodplain deposits are ordinated into bins from 1 (representing the youngest deposits next to the active channel) to n (representing the oldest floodplain material) (Fig. 3, G to I). Note that this exercise of mapping cross-cutting relationships is particularly well suited to Arctic rivers (Fig. 3), both because the floodplain vegetation tends to be less dense than in tropical settings, and because the vegetation correlates strongly with topography on the alternating levees and swales in scroll bar complexes (*30*), which amplifies the visual contrast of the geomorphic patterns.

2) Geochemical age constraints. To convert the relative terrain ages from step 1 into absolute ages, we sampled floodplain material for radiocarbon (^{14}C) and optically stimulated luminescence (OSL) analyses. In total, we measured 175 stratigraphic sections through the near-surface floodplain stratigraphy: $n = 46$ in Beaver, $n = 43$ in Huslia, and $n = 86$ in Alakanuk (Fig. 3, A to C). The ^{14}C and OSL data from Huslia were published in (*30*); the data from Beaver and Alakanuk are new to this study (*32*). Where layers of coarse organic carbon, particularly woody debris, were present in the primary floodplain stratigraphy, we collected samples for ^{14}C analysis. We avoided plant roots and other material associated with the modern floodplain biosphere. Where layers of well-sorted sands were present in the fluvial stratigraphy, we collected samples for OSL analysis. Details of sample collection, processing, and analysis are described in Materials and Methods and Supplementary Text.

3) Probabilistic conversion from relative to absolute ages. The geochemical sampling led to $n = 19$, $n = 44$, and $n = 25$ ^{14}C and OSL age constraints at the Beaver, Huslia, and Alakanuk field sites, respectively (Fig. 3). Next, we used these observations to establish our best estimate for the age and uncertainty of each relative age unit. Note that the temporal ordination of the relative age units imposes an additional constraint that we can incorporate into our age model. For example, the relative age unit 3 must be older than unit 2 and younger than unit 4. Using Markov chain Monte Carlo (MCMC) methods (*33*), we generate estimates for the age and uncertainty of each mapped unit (Fig. 3, J to L).

Governing equations linking the age of floodplain deposits and the age of exported river sediments

We are interested in quantifying three interrelated quantities: (i) the age of sediment observed on the floodplain (which represents our ground-truth observables in Fig. 3), (ii) the age of sediment eroded from the floodplain (which represents the floodplain storage time distribution), and (iii) the age of sediment exported by the river (which represents the age of particles that have undergone n sequential storage and release events) (Fig. 1A). As summarized in (*17*), mass balance quantitatively links (i) and (ii); at steady state, the age distribution of particles being eroded by the river must exactly match the distribution of sediments achieving that same age on the floodplain (via aging). This condition requires that the probability density function (PDF) of the age of particles residing on the floodplain, $g(t)$, is linked to the cumulative distribution function (CDF) of the age of particles being eroded by the river, $F(t)$, as

$$g(t) = \frac{Q_l}{M_0}[1 - F(t)] \tag{3}$$

where M_0 (M) is the total mass of floodplain sediment and Q_l ($M\ T^{-1}$) is the sediment exchange resulting from lateral migration of the river (*17*). Equation 3 provides a way to translate observations of floodplain terrain ages (Fig. 3) into estimates of the ages of eroded sediment.

Note that $F(t)$ reflects the distribution of storage times for a single storage event in the floodplain. In the total transport journey from source to sink (Fig. 1A), a particle will be repeatedly stored in floodplain deposits, then eroded and liberated in the channel to be transported downstream some distance x_{tran}, and then deposited in the floodplain again. Because the transit time is dominated by the intervals when the particle is stored in floodplain deposits, rather than in transit along the river channel (*4*), the age of the particles transported by the river can be approximated as

$$h(t) = f(t)^{*n} \tag{4}$$

where $f(t)$ is the PDF of storage times for a single storage event, n is the number of storage events, and the symbol * denotes convolution (*4*). Note that n scales linearly with the river length, L

$$n = \frac{L}{x_{tran}} \tag{5}$$

where x_{tran} is the characteristic transport length between storage events. A key to implementing Eqs. 4 and 5 in practice is constraining the transport lengthscale, x_{tran}. We can estimate x_{tran} using mass balance to link Q_l with the channel migration rate

$$Q_l = \rho_b M_{avg} H x_{tran} \tag{6}$$

where ρ_b is the sediment bulk density ($M\ L^{-3}$), M_{avg} is the reach-averaged channel migration rate ($L\ T^{-1}$), and H is the channel depth (L). Q_l represents the component of the downstream sediment discharge that is tied up with the downriver lateral migration of the river, not the total sediment discharge of the river (Q_s). As a simple starting point, we follow (*4*) and hypothesize that Q_l and Q_s are proportional to each other

$$Q_l \propto Q_s \tag{7}$$

where we expect the coefficient of proportionality to be sensitive to factors such as the distribution of particle grain sizes that constitute the floodplain versus the riverine sediment load. For example, a river's downstream sediment discharge could be dominated by mud, whereas the sediment in the floodplain reservoir may be predominantly composed of sand (*34*, *35*). In this case, the muddy "washload" component of Q_s largely may not participate in the sediment exchange associated with lateral migration of the river and therefore should be excluded from Q_l [but cf. (*36*)]. Volumetric observations of sediment exchange into and out of the riverbanks [e.g., from time-lapse light detection and ranging (LiDAR) surveys (*37*, *38*) or subpixel measurements of satellite imagery (*27*)], in concert with measurements of the through-going riverine sediment fluxes (*34*),

allow one to constrain the relative scaling between Q_l and Q_s (*39*). Here, we proceed with a generic proportionality. Rearranging Eqs. 6 and 7 gives an expression for x_{tran} (L), expressed here as a lengthscale that is normalized by the channel width

$$\frac{x_{tran}}{W} \propto \frac{Q_s}{\rho_b M_{avg} W H} \tag{8}$$

The term on the right-hand side can be simplified through the definition of the sediment transport rate, q_s ($L\ T^{-1}$)

$$q_s = \frac{Q_s}{\rho_b W H} \tag{9}$$

which makes the normalized transit lengthscale simplify to

$$\frac{x_{tran}}{W} \propto \frac{q_s}{M_{avg}} \tag{10}$$

Empirical observations of sediment transport in natural rivers suggest that the channel migration rate (M_{avg}) scales quasi-linearly with the total sediment transport rate (q_s) (*39*–*41*), suggesting that the normalized transit lengthscale $\frac{x_{tran}}{W}$ could be well conserved across channels with a broad array of sizes and migration rates (*4*). For example, Fig. 4A shows data for modern rivers in the Amazon basin (*39*), illustrating an approximately linear scaling $q_s \propto M_{avg}$. For the data in Fig. 4A, the normalized transit lengthscale $\left(\frac{x_{tran}}{W}\right)$ is relatively narrowly distributed around a mean of 320 (channel widths) or ~32 meander bends (Fig. 4B). In summary, using Eqs. 3 to 10, one can translate observations of the age distribution of floodplain sediments (Fig. 3) to quantitative estimates of the floodplain storage time and the age distributions of sediment transported downriver.

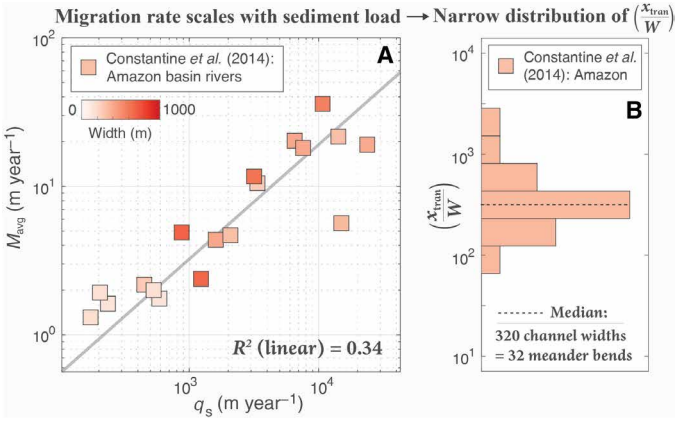

Fig. 4. Sediment flux, migration rates, and transit lengthscales estimated for modern rivers. (**A**) Observations from major rivers in the Amazon basin (*39*) support a quasi-linear scaling between the sediment transport rate [q_s (meters per year)] and the average channel migration rate (meters per year). (**B**) The quasi-linear relationship in (A) supports a relatively well-conserved sediment transport lengthscale, x_{tran}/W, which does not show systematic residual trends with channel size or migration rate. The distribution in (B) has a mean of 320 (channel widths) and an interquartile range (25th to 75th percentile) of 210 to 440 channel widths. Observations of the geometry of modern meandering rivers (see the Supplementary Materials) indicate that the average length of a meander bend is 10.0 ± 1.4 channel widths. Thus, in the distribution shown in (B), x_{tran} has a mean value of 32 bends (interquartile range: 21 to 44 bends). Note that the x_{tran} values shown in (B) assume a proportionality coefficient of 1 in Eq. 10.

Numerical simulations of meander evolution

The field observations in Fig. 3 provide three snapshots of floodplain age distributions from rivers with a diverse set of morphologies and a range of migration rates. However, to systematically explore how variables such as the channel width, average migration rate, and total floodplain width affect the final age distributions, we need more than $n = 3$ observations.

We use numerical simulations to explore the long-timescale behavior of meandering river systems (*4*, *17*, *42*, *43*) with a range of channel sizes and migration rates. We use the convolutional model of Howard and Knutson (*29*), which successfully describes the meander kinematics observed at our field sites (*27*, *44*) (see the Supplementary Materials), as well as meandering rivers around the world (*20*, *40*). Note that we focus on floodplain construction through lateral accretion (rather than overbank deposition) because the lateral accretion deposits dominate the mass of the floodplain reservoir (see Supplementary Text). However, for some applications, the overbank deposits may play an outsized role due to their abundance of fine grains (and associated organic carbon, particle-bound contaminants, etc.). We explore these caveats in the Discussion and Supplementary Text. An example meander simulation is shown in Fig. 1B. We perform $n = 600$ simulations spanning an array of parameter values including channel widths (W = 50 to 1000 m), migration rates (M_{avg} = 0.1 to 20 m/year), friction coefficients C_f [a parameter that affects the meander kinematics (*29*)], and model runtimes [t = 10 kyr to 10 million years (Myr)]. At the end of each simulation, we measure the age distribution of floodplain sediments (e.g., Fig. 1B). Our goal is to evaluate whether the resulting age distributions from the $n = 600$ simulations can be rescaled to collapse into a simple functional form.

RESULTS

Three distinct scaling regimes revealed by meander simulations

Across all model experiments, the age of the simulated floodplain collapses to a single distribution (Fig. 5) if we rescale the model time by τ_w (the time it takes the river to migrate a distance of one channel width). As hypothesized, Fig. 5 reveals three distinct scaling regimes. At the shortest timescales (i.e., those shorter than $\sim 5\tau_w$), floodplain sediments have the highest probability of being observed on the floodplain. This is because meander kinematics dictate that, on these short timescales, the channel tends to be migrating away from the point of interest. At a timescale of ~5 to 10 τ_w, there is a transition whereby meander bend expansion and cutoff (*18*) alter the statistical behavior of the river's motion from being roughly unidirectional to behaving similarly to a random walker (*17*, *19*). A consequence of this random-walk (diffusion-like) behavior is that older sediments become less probable but in a heavy-tailed manner (i.e., the oldest sediments are more probable than would be predicted from a model of exponential decay) (*4*, *17*). Last, at sufficiently long timescales, tectonic history and regional constraints on the size and shape of the floodplain (*19*) require that the abundance of the oldest sediments falls toward zero (Fig. 5).

A simple scaling equation to describe the age distribution of alluvial sediments

The simplest functional form that captures the behavior in Fig. 5 is a broken power law (*45*) with three regimes. According to this model, the PDF of the age of floodplain sediments can be described as

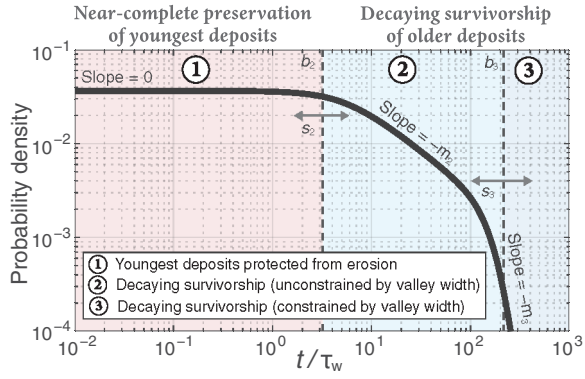

Fig. 5. PDF describing the age distribution of the floodplain. Data from $n = 600$ numerical simulations (Fig. 1C), each run to statistical steady state, collapse to support a similarly shaped distribution if the model time t is rescaled by a critical timescale $\tau_w = W/M_{avg}$. See the Supplementary Materials for an illustration of the empirical PDFs of individual numerical simulations. The observations are fit with a broken power law (Eq. 11). The best-fit parameters are $b_2 = 5.38$, $b_3 = 211$, $m_2 = 0.636$, $m_3 = 7.92$, $s_2 = 0.613$, and $s_3 = 0.305$. The same distribution shown here is repeated in Fig. 6A, where it is combined with Eqs. 3 to 8 to construct Fig. 6 (B and C).

$$g(\tau) = a\left[1+\left(\frac{\tau}{b_2}\right)^{1/s_2}\right]^{-m_2 s_2}\left[1+\left(\frac{\tau}{b_3}\right)^{1/s_3}\right]^{-m_3 s_3} \quad (11)$$

where τ is the dimensionless age of the floodplain material, calculated as $\tau = t/\tau_w$. The parameters b_2 and b_3 represent the positions of the scaling breaks (Fig. 5). The parameters s_2 and s_3 describe how gradually versus abruptly the function transitions between the different power-law segments. Last, the parameters m_2 and m_3 denote the power-law slopes of segments ② and ③ in Fig. 5. The slope of the first segment, ①, is zero (Fig. 5). In total, there are six independent parameters in Eq. 11. The parameter a is simply a normalizing factor that ensures the integral of $g(\tau)$ is one.

We find that the parameters describing segments ① and ② of the broken power law (Fig. 5) are well conserved across the $n = 600$ simulations. These segments define the internal dynamics of the meandering river. The parameters defining segment ③ (particularly the scale-break parameter b_3) reflect the interaction of the channel with the confining valley geometry (*17*) or the long-term subsidence behavior (Fig. 1C). In the no-subsidence end-member, the position of the scale break b_3 can be estimated as $b_3 = \tau_{max}/\tau_w$, where τ_{max} represents the time it would take the channel to traverse the full width of the observed floodplain (W_f) (see the Supplementary Materials)

$$\tau_{max} \approx \frac{W_f}{M_{avg}} \quad (12)$$

To summarize, the broken power-law model (Eq. 11) allows one to predict the three interrelated age distributions of (i) the material persisting on the floodplain (Fig. 6A), (ii) the material removed from the floodplain via erosion (Fig. 6B), and (iii) the material exported downriver (Fig. 6C), as a function of the channel width and average migration rate, parameters that are readily obtained for any large river in the world from satellite data (*20*, *21*, *25*–*27*, *39*, *44*).

Here, we test whether the broken power-law model in Fig. 5 successfully reproduces the observed age distributions at our field sites (Fig. 3). To apply the model to all three field examples, we need a framework for extending the model from single-threaded to anastomosing and distributary meandering systems. A simple approach for doing so is to decompose a multichannel meandering system into its set of constituent channels, each with different width, length, and average migration rate (and therefore a different floodplain age PDF in Fig. 5). We hypothesize that one can estimate the overall age distribution of the floodplain as an average of the individual PDFs, weighted by the amount of geomorphic work (floodplain area or volume processing rate) done by each channel (Fig. 7). Note that we pose this methodology as a hypothesis because it is possible that interactions (attraction, capture, etc.) between the different threads of an anastomosing or distributary meandering system could affect the resulting floodplain age distributions. In addition, an implicit assumption of this approach is that the number and size of channels in a multichannel system have remained statistically similar to the present day over the life of the floodplain. This assumption may be violated in scenarios in which the floodplain is undergoing major change. Also note in Fig. 7 that we can define the geomorphic work in terms of either area or volume. The total area reworking rate ($L^2\ T^{-1}$) from all i strands of a multichannel system is $\sum_i L_i M_{avg,i}$, where L and M_{avg} are the length and average migration rate, respectively. Meanwhile, the total volumetric reworking rate ($L^3\ T^{-1}$) from i strands of a multichannel system is $\sum_i L_i M_{avg,i} H_i$, where H is the channel depth. One would use the area-based weighting for predicting mapped floodplain age distributions similar to those in Fig. 3, but volume-based weighting for predicting the age distribution of sediment transported and exported by the river (Fig. 8, B and C). If no in situ observations are available, then channel depth (H) can be estimated from channel width (fig. S2). See Supplementary Text for a graphical illustration of this workflow and a step-by-step guide for implementing it. Keeping all of the aforementioned caveats in mind, this simple workflow implies that if we measure the length, width, and average migration rate of each channel, as well as the total width of the floodplain, W_f, then we can predict the overall age distribution of the alluvial deposits. We test this hypothesis by predicting the age distributions of the sites in Fig. 3.

Without tuning, the model correctly predicts the floodplain age distributions from all three sites. At Beaver, AK, the observed floodplain age CDF is $y = (0.36 \pm 0.05)x^{(0.53\pm0.09)}$, and the predicted floodplain age CDF is $y = (0.32 \pm 0.02)x^{(0.57\pm0.03)}$ (where x represents the age in kyr) (Fig. 7D). The observed and predicted age models are within error of each other. The same is true for the other two sites. At Huslia, AK, the observed floodplain age CDF is $y = (0.24 \pm 0.02)x^{(0.47\pm0.04)}$, and the predicted floodplain age CDF is $y = (0.27 \pm 0.01)x^{(0.47\pm0.02)}$ (Fig. 7E). Last, at Alakanuk, AK, the observed floodplain age CDF is $y = (0.51 \pm 0.07)x^{(0.81\pm0.16)}$, and the predicted floodplain age CDF is $y = (0.49 \pm 0.01)x^{(0.78\pm0.02)}$ (Fig. 7F).

DISCUSSION

Implications for floodplain storage timescales

The scaling laws in Fig. 6 suggest that the typical time a particle spends trapped in a floodplain reservoir does not depend on the absolute size (i.e., width) of the channel or on the absolute rate of channel migration, but rather on the ratio of those two quantities ($\tau_w = W/M_{avg}$). For

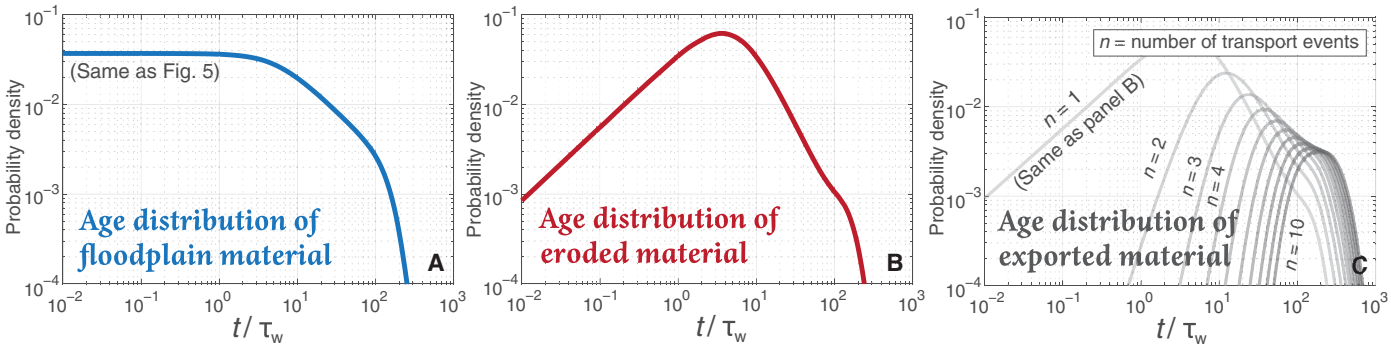

Fig. 6. Interrelated age distributions of stored, eroded, and exported alluvial particles. (**A**) Floodplain age PDF, repeated from Fig. 5. (**B** and **C**) PDFs of the (B) storage time distribution and (C) age of the exported material. As described in the main text, mass balance quantitatively links the distributions in (A) and (B) (see Eq. 3). Recall, however, that this linkage between the distribution of floodplain sediment ages with its corresponding distribution of eroded sediment is based on an assumption of steady state. The distribution in (C) represents the convolution of the distribution in (B) with itself *n* times, where *n* is the number of sequential storage and transport events (see Eq. 4) (*4*). On the *x* axis, the time is rescaled by the critical timescale τ_w, which represents the time it takes a channel to erode the distance equivalent to one channel width.

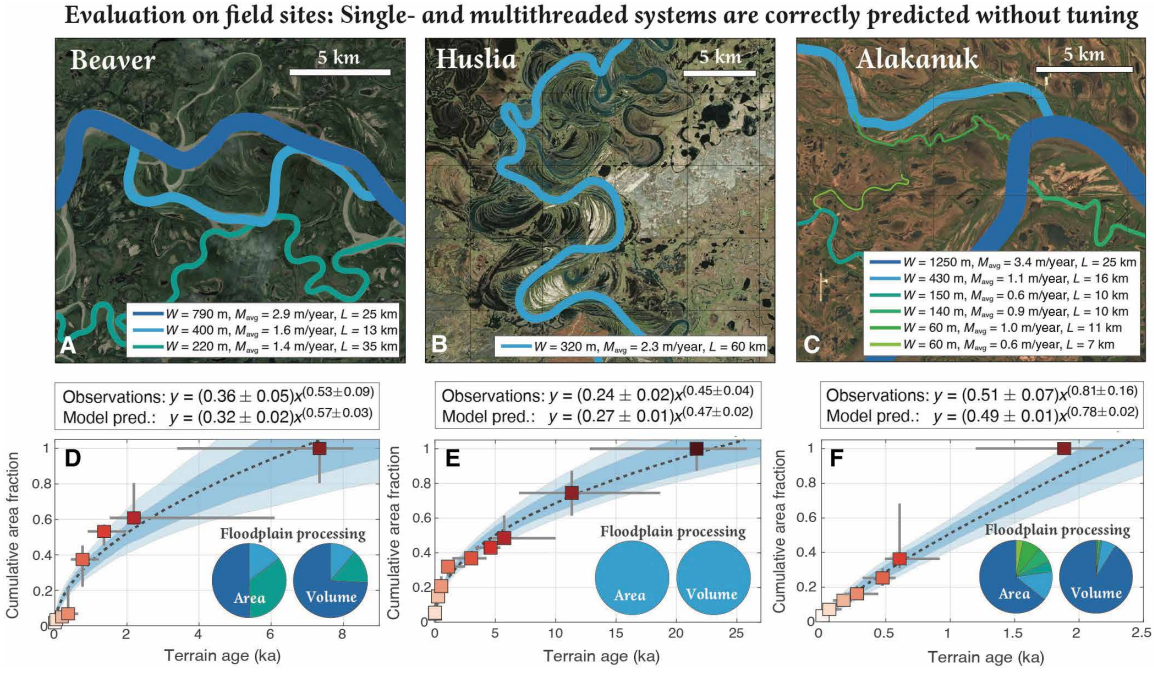

Fig. 7. A test to evaluate whether the broken power-law model can correctly predict the floodplain age distributions at our three field sites (Fig. 3). (**A** to **C**) To generate the model predictions, we decompose each river system into a series of threads and then measure the length, width, and average migration rate (*44*) of each thread. Following the workflow outlined in Supplementary Text, we calculate the floodplain age distribution that would result from each thread and then sum the distributions according to their geomorphic work (floodplain area processing rate). Last, we convert the resulting PDF to a CDF. We fit the CDF with a simple low-parameter function of the form $y = ax^b$. The legends in (**D**) to (**F**) compare the observed and predicted floodplain age-area relationships. The observed age-area relationships are based on fitting a $y = ax^b$ function to the cumulative age-area data from the age maps in Fig. 3. In all three cases, the model predicts the observed age-area relationships within uncertainty. Note that there are no tunable parameters in the model; the parameter values from Fig. 5 are used directly (except for b_3, which is calculated as the ratio of the total study-area width to the channel migration rate—see Eq. 12). In Fig. 8 (A to C) and Supplementary Text, we describe how one can convert the age distribution of sediments on the floodplain (i.e., the observed quantity from Fig. 3) to estimates of the age distribution of eroded sediments (which represents the floodplain storage time distribution) and the age distribution of transported/exported sediments. In [(D) to (F)], the colors of the squares denote the floodplain age unit, following the legend shown in Fig. 3 (J to L).

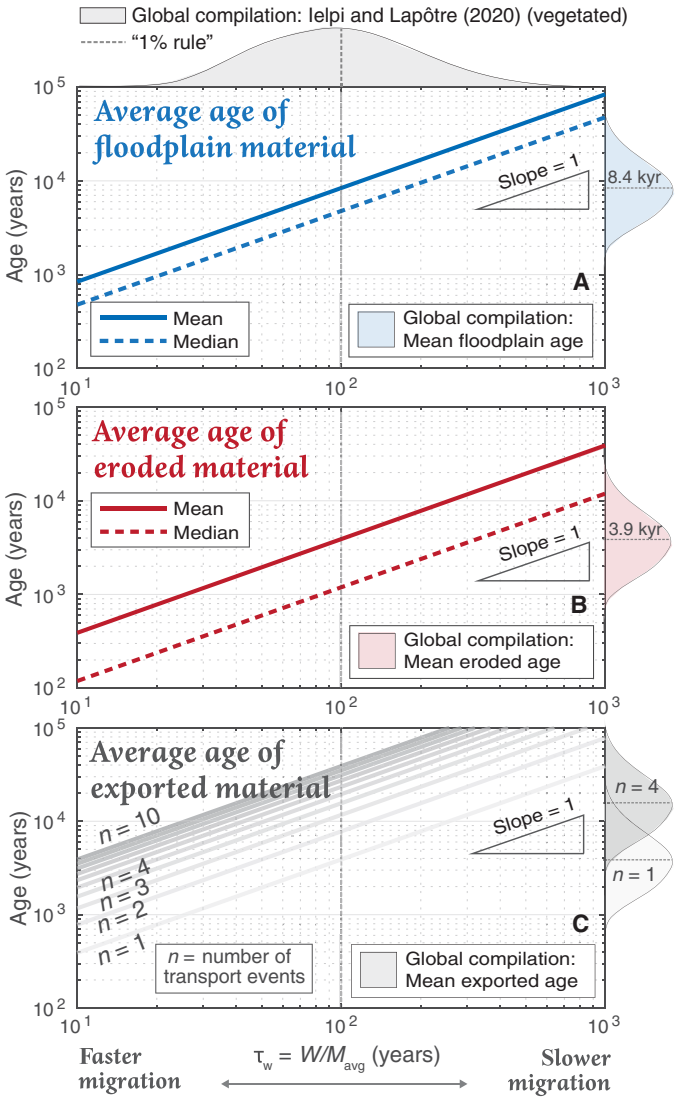

Fig. 8. An illustration of how the ratio of the channel width to the migration rate (τ_w) controls the age of stored, eroded, and exported alluvial particles. In (**A**) to (**C**), we apply the distributions in Fig. 6 [which are constructed from the broken power-law model in Fig. 5, using an upper scale break of $b_3 = \tau_{max} = 200$] to compute the particle age distributions as a function of τ_w. We compute the mean and median ages of the (A) material on the floodplain, (B) material eroded from the floodplain, and (C) material exported by the river after *n* sequential storage and transport events. The shaded distribution on the *x* axis shows the global compilation from (*23*) (vegetated rivers), which suggests that rivers tend to erode between 10 and 0.1% of their width per year, corresponding to characteristic timescales (τ_w) of 10 and 1000 years, respectively. In (A), the curve representing the mean age is described by the equation $y = 84\tau_w$, and the curve representing the median age is described by the equation $y = 48\tau_w$. In (B), the curve representing the mean age is described by the equation $y = 39\tau_w$, and the curve representing the median age is described by the equation $y = 12\tau_w$.

example, a 1000-m-wide river migrating 10 m/year and a 10-m-wide river migrating 0.1 m/year tend to produce floodplains with the same age distributions. Figure 2A shows typical values of τ_w for modern rivers on Earth (*21*–*23*). The distributions in Fig. 2A are centered around a peak of $\tau_w \approx 100$ years. This peak value is equivalent to the so-called "1% rule," a long-standing rule of thumb in geomorphology that alluvial rivers tend to erode about 1% of their width per year (*46*, *47*).

Figure 8 summarizes the relationship between τ_w and the average ages of alluvial particles. Rivers obeying the 1% rule produce floodplains with mean and median ages of 8.4 and 4.8 kyr, respectively (Fig. 8A), and mean and median eroded sediment ages of 3.9 and 1.2 kyr, respectively (Fig. 8B). Rivers obeying a 2% rule ($\tau_w = 50$ years) produce floodplains with mean and median ages of 4.2 and 2.4 kyr, respectively, and mean and median eroded sediment ages of 1.9 and 0.6 kyr (Fig. 8). Our three field sites lie near the center of the distribution for global rivers, with mean floodplain ages of 2.8, 6.0, and 1.1 kyr, at Beaver, Huslia, and Alakanuk, respectively (Fig. 7).

Implications for contaminant remediation and removal

One implication of Fig. 8 is the unexpected conclusion that large and small rivers—for example, the large Sacramento River storing Hg-contaminated sediments from historical gold mining in the Sierra (*13*) and the small Little Wind River reworking U-contaminated sediments at the Department of Energy site at Riverton, Wyoming (*48*)—may trap and store contaminants in their floodplains for similar lengths of time (*10*–*13*). The scaling equations in this study provide a framework for calculating the characteristic storage and transport timescales for a particular site or system of interest.

The application of contaminant remediation raises a number of potentially important caveats that should be considered when interpreting the results in Fig. 8. The first has to do with the distinction of how the floodplain construction proceeds via lateral accretion versus overbank deposition (*49*). In both the numerical meander simulations (Fig. 1B) and the field mapping (Fig. 3), we define the age of the floodplain based on the age of the LASs (fig. S8). We do this for two reasons. The first is that, at our three field sites, the lateral accretion deposits represent most of the mass of the floodplain reservoir (constituting an estimated ~80 to 90% of the total mass—see Supplementary Text). The second reason is that we observe the most rapid rates of overbank deposition in the time interval immediately following when the river migrates away from a point of interest. For example, at our three field sites (Fig. 3), an estimated two-thirds of the total observed overbank deposition occurs within one τ_w of the age of the LAS, meaning that the age distribution of the LASs (Fig. 6) may also capture (to first order) the age distribution of the overbank deposits.

Another caveat to our model is that we assume that the subsidence rate and river avulsion frequency are low enough that the river can rework the recent floodplain deposits (*49*). If avulsions are frequent, then the river may jump into an area of the floodplain that has a very old terrain (*49*). Thus, on large distributary systems such as megafans or coastal plains, the analysis presented here may only apply to the active lobe (*50*); older abandoned lobes or channel belts would age in place.

Implications for Earth history

A final implication of the scaling relations in Fig. 8 is that perturbations that cause an increase in relative channel migration rates (*23*, *27*, *39*, *51*–*53*) may invoke a concomitant decrease in floodplain storage durations. This inverse correlation between migration rates and storage durations may have important ramifications for understanding sedimentological, chemical weathering, and carbon cycle changes in Earth's history (*54*). For example, the Paleocene-Eocene Thermal Maximum (PETM), a greenhouse event that occurred ~56 Myr ago, is thought to have radically altered fluvial systems (*55*) and the intensity of chemical weathering on river floodplains (*54*).

Specifically, higher discharge seasonality (*53*) and/or increased sediment production from mountain catchments (*55*) appears to have driven more rapid fluvial reworking during the PETM. All else being equal, Fig. 8 predicts that when migration rates increase, particles have less time to undergo chemical weathering in floodplain reservoirs (*5*–*8*). This negative feedback should act to mute the increase in floodplain chemical weathering expected from the high P_{CO_2} and temperature during the PETM. This prediction is consistent with geological/geochemical observations (*54*) that the weathering response during the PETM was muted in proximal fluvial facies (i.e., floodplain sediments that are frequently reworked by the active channel) relative to distal cumulative soils (*54*).

Drawing upon another example from Earth's history, we note that Fig. 8 points to a positive feedback loop that may have helped establish the change in river floodplain architecture that occurred during the greening of the continents roughly 400 Myr ago (*51*, *56*). The Paleozoic evolution of land plants, which has been hypothesized to stabilize river channels and slow migration rates (*23*, *51*), is coeval with an unparalleled and unidirectional upsurge in the proportion of mudrock preserved in the geological record (*56*). A slowdown in river migration associated with land plants—either due to direct riverbank stabilization from rooting (*23*, *51*) or from indirect effects such as increased floodplain retention of fine-grained sediment due to plant-derived organics (*57*)—causes the floodplain storage timescale to increase. Particles persisting on the floodplain for longer timespans can undergo further physical and chemical weathering (including clay formation) (*5*–*8*), promoting a positive feedback with muddier floodplains and yet slower channel migration rates (*58*, *59*), perhaps enabling the stabilization of a new type of floodplain architecture roughly 400 Myr ago (*51*, *56*).

Of course, both of the aforementioned examples—the climatic perturbation in the case of the PETM and the secular state change in the case of the evolution of land plants—likely invoked adjustments not only in the average channel migration rates but also in the hydraulic geometry (e.g., width, depth, and slope) (*35*), the planform style (e.g., single-threaded meandering versus multithreaded braided or anastomosing) (*35*), and the avulsion frequency (*53*, *55*). All of these changes may influence the floodplain storage timescale in ways that are not well captured by the simplest version of our model summarized in Fig. 8.

Application of the model

Keeping the assumptions and limitations of the model in mind, we now turn to its utility and opportunity. Perhaps most importantly, the model only relies on three characteristics—the channel migration rate, the channel width, and the floodplain width. These parameters are readily obtained for any large river in the world from field observations (*60*) or satellite imagery (*21*, *25*). Thus, it may now be tractable to quantify the timescales for terrestrial sediment storage and transport at a global scale, with implications for topics such as (i) the fate of terrestrial organic carbon (*1*–*3*) (i.e., how much organic carbon is oxidized during riverine transit versus delivered to ocean deltas, where it has a high chance of sequestration on geological timescales) (*61*, *62*), (ii) the style and efficiency of continental chemical weathering (*5*, *6*, *8*, *9*), (iii) the buffering or shredding of environmental signals preserved in the geological record (*14*–*16*), and (iv) the timescales for contaminant persistence and removal from floodplain ecosystems (*10*–*13*). The efficient description of meander kinematics presented here provides a scalable basis from which to quantify sediment, carbon, nutrient, and contaminant cycling in floodplain landscapes on timescales ranging from years to millions of years.

MATERIALS AND METHODS

Field sampling

We measured 175 stratigraphic sections through the near-surface floodplain stratigraphy: $n = 43$ in Huslia (65.700°N, 156.387°W), $n = 46$ in Beaver (66.362°N, 147.398°W), and $n = 86$ in Alakanuk (62.685°N, 164.644°W) (see Fig. 3) over the course of four field campaigns (May to June 2021, September to October 2021, May to June 2022, and September to October 2022). To constrain the ages of the fluvial deposits, we collected samples for ^{14}C and OSL dating. The ^{14}C and OSL data from Huslia were previously published in (*30*); the data from Beaver and Alakanuk are new to this study (*32*). Where layers of coarse organic carbon, particularly woody debris (e.g., rafts of small sticks), were present in the primary floodplain stratigraphy, we collected a sample for ^{14}C analysis. We avoided bulk sediment for ^{14}C measurements because bulk sediment contains a mixture of biospheric organic carbon and petrogenic organic carbon ("^{14}C dead" carbon that does not reflect the deposit age and will tend to bias the age estimates older). We acquired the ^{14}C samples using metal trowels or tweezers while wearing latex gloves. Samples were placed in Whirl-Pak bags and stored frozen until analysis. Where layers of well-sorted sands (fine sand, medium sand, or coarse sand) were present in the fluvial stratigraphy, we collected a sample for OSL analysis. We placed a dark tarp over the "outcrop" (the exposed riverbank) to avoid exposure to sunlight, used a shovel to dig back the wall of the riverbank, and then used a rubber mallet to pound a 2-inch (5.1-cm)–wide opaque black polyvinyl chloride or aluminum pipe into the sand. We covered the ends of the tube with black vinyl end caps, wrapped in duct tape, and stored in a dark, cool place until analysis.

^{14}C analysis

Samples were rinsed with Milli-Q water and stored in combusted glass vials before being sent to the Keck radiocarbon facility at the University of California, Irvine. ^{14}C ages are reported as fraction modern and uncalibrated ^{14}C years [before present (B.P.)]. We converted the $\Delta^{14}C$ observations to calibrated ages (cal B.P., defined as years before 1950) using CALIBomb (*63*). We used the Intcal20 curve for prebomb samples and the Northern Hemisphere Zone 1 curve for postbomb samples (*63*).

OSL analysis

Samples were analyzed for quartz OSL at the University of Texas at Arlington (UTA) Luminescence Laboratory. A subset of six samples was also prepared for K-feldspar post-infrared infrared stimulated luminescence (post-IR IRSL) analysis at UTA. Laboratory procedures for the OSL data used for Huslia, AK, are described in (*30*). See the Supplementary Materials for figures illustrating the single-grain dose distribution data and the resulting age estimates.

Geomorphic mapping

We develop a chronology of the relative floodplain age by using cross-cutting relationships, starting at the position of the active channel and working backward to the oldest deposits in the landscape. The result of this cross-cutting analysis is a relative age map,

with units ordinated from 1 to n, where n is the oldest unit (Fig. 3). Within individual cross-cut age units, scroll bar sequences provide an additional (superimposed) age constraint. We annotate these subdivisions in the terrain maps (Fig. 3) but stick to $n \approx 10$ terrain age units so that each unit has geochemical age constraints.

From relative to absolute ages

We use the ^{14}C and OSL ages (*32*) to convert the relative age units to absolute ages in units of cal kB.P. [cal kyr before the present (i.e., 1950); using the standard ^{14}C terminology where cal B.P. is defined as years before 1950]. Our varied ^{14}C and OSL samples within each relative age unit (typically $n = 1$ to 14 samples—see Fig. 3) provide one representation of the mean age and associated uncertainty of each relative age unit. However, sometimes we only have $n = 1$ sample from a given relative age unit. Moreover, the temporal ordination constructed from the cross-cutting relationships provides a strong constraint on the possible age of each unit (which must be bounded by the ages of the older and younger units). The constraint imposed by this temporal ordination is often applied in an MCMC framework to construct stratigraphic age models (*33*). Here, we apply the same approach to the age models in Fig. 3. We use the geochemical samples to define the prior age distributions for each relative age unit and then use MCMC (*33*) to find $n = 2000$ paths through the age model that satisfy the temporal ordination constraints. The resulting MCMC age models (median with shaded 25th to 75th and 5th to 95th percentiles) are shown in gray in Fig. 3 (G to I).

Linking the ages of particles eroded by the river versus those persisting on the floodplain

As described in the Introduction, we are interested in quantifying three interrelated quantities (Fig. 8): (i) the age distribution of sediment residing on the floodplain; (ii) the age distribution of sediment being eroded from the floodplain via active river migration; and (iii) the age distribution of particles transported by the river. These particles have undergone n sequential floodplain storage and transport events (*4*).

Because the timescale of floodplain storage (~10^3 years) is much greater than the timescale of downstream riverine transport (~10^1 days), the age distribution of (iii) is simply the nth convolution of the age distribution of (ii) (Eq. 4) (*4*). Likewise, the age distributions of (i) and (ii) are linked quantitatively at steady state through reservoir theory (*17*), as described below. In the following section, the values in parentheses denote the dimensions of each variable, where (M) = mass, (T) = time, and (L) = length.

Following the nomenclature of Bradley and Tucker (*17*), let $M(t)$ (M) represent the mass of sediment on the floodplain that has age t or younger. The CDF of the age of particles residing on the floodplain, $G(t)$, is given by

$$G(t) = \Pr(T \le t) = \frac{M(t)}{M_0} \tag{13}$$

where Pr() represents the probability, T is a random variable denoting the age of a sedimentary particle on the floodplain, and M_0 (M) is the total mass of floodplain sediment (*17*). The CDF $G(t)$ approaches 0 in the limit $t \to 0$ and 1 in the limit $t \to \infty$. The derivative of $G(t)$ with respect to the particle age, t, gives the PDF for the age distribution of particles residing on the floodplain, $g(t)$

$$g(t) = \frac{d}{dt}G(t) = \frac{1}{M_0}\frac{d}{dt}M(t) \tag{14}$$

Following (*17*), we define analogous CDF and PDF equations to describe the age distributions of particles being eroded by the river (i.e., removed from the floodplain via riverbank erosion). Let $Q(t)$ ($M\ T^{-1}$) represent the mass flux of sediment with age t or younger being eroded by the river. By analogy with Eq. 13, the CDF of this age distribution of eroded sediment, $F(t)$, is

$$F(t) = \Pr(T \le t) = \frac{Q(t)}{Q_l} \tag{15}$$

where Q_l ($M\ T^{-1}$) is the component of the sediment discharge of the river that is tied up with lateral channel migration (Eq. 6). Last, the PDF of the age distribution of eroded sediment, $f(t)$, is

$$f(t) = \frac{d}{dt}F(t) = \frac{1}{Q_l}\frac{d}{dt}Q(t) \tag{16}$$

At steady state, the age distributions of both the sediment residing on the floodplain, $M(t)$, and the sediment being eroded by the river, $Q(t)$, must be constant with time. For this constraint to hold, in each timestep, the age distribution of sediment being eroded by the river must exactly be replaced via the aging of sediments on the floodplain

$$Q_l - Q(t)\frac{d}{dt}M(t) = M_0 g(t) \tag{17}$$

Rearranging Eq. 17 yields a relation for steady state that directly links the PDF of the age of particles residing on the floodplain, $g(t)$, with the CDF of the age of particles being eroded by the river, $F(t)$

$$g(t) = \frac{Q_l}{M_0}[1 - F(t)] \tag{18}$$

which is the relation shown in Eq. 3.

Numerical simulations of river meandering

We implement the curvature-driven meander model of Howard and Knutson (*29*), which successfully describes the meander kinematics at our three field sites (*27*, *44*), as well as rivers around the world (*20*, *40*). According to this model, the bank migration rate, $M(s)$, is

$$M(s) = \Omega M_0(s) + \left[\Gamma \int_0^\infty M_0(s-\zeta)G(\zeta)d\zeta\right]\left[\int_0^\infty G(\zeta)d\zeta\right]^{-1} \tag{19}$$

where s is the along-river coordinate system (longitudinal distance), ζ is the distance upstream from the point of interest, and $G(\zeta)$ is a weighting function that decays exponentially upstream from the point of interest

$$G(\zeta) = e^{-\alpha\zeta} \tag{20}$$

The α term in Eq. 20 describes how the influence of the channel curvature decays with increasing distance upstream from the point of interest. This decay term can be parameterized as a function of the friction factor, C_f (dimensionless), and the water depth, H (L) (*20*, *29*)

$$\alpha = 2C_f / H \tag{21}$$

The term $M_0(s)$ represents what Howard and Knutson (*29*) refer to as the "nominal" migration rate; that is, the rate that would be observed if migration were only a function of local curvature. The simplest functional dependence for $M_0(s)$ is

$$M_0(s) = k\left(\frac{W}{R}\right) \tag{22}$$

where k ($L\ T^{-1}$) is a migration rate constant, W (L) is the channel width, and R (L) is the local radius of curvature (*29*). We refer to the dimensionless ratio W/R as the "local normalized curvature." In Eq. 19, Ω and Γ are constants (-1 and 2.5, respectively) (*29*).

Quantifying cutoff timescales in modern and simulated rivers

In fig. S1 and Fig. 2, we present a relationship between τ_w and τ_{cut} based on the numerical meander simulations (*29*). To validate this scaling, we turn to observations of modern meandering rivers. We use Landsat satellite observations on Google Earth Engine from 1984 to 2022 (a 39-year period) to identify cutoff events for 48 river reaches across the world. We focus on regions in Alaska, the Amazon, and Papua New Guinea, where large rivers are relatively unaffected by dams or erosion-control structures. The premise of this analysis is that, although the cutoff timescales (τ_{cut}) for an individual meander loop are long [on the order of 10^3 years (Fig. 2)], a river reach with $n = 100$ bends, for example, is likely to have experienced multiple cutoff events in the past 40 years. In other words, the low probability of cutoff for a single meander loop can be compensated by analyzing longer reaches with more consecutive meanders. In total, we inventory 15,808 km of river length and identify 213 cutoff events (see the Supplementary Materials). We distinguish neck cutoffs and chute cutoffs in the historical inventory because our numerical meander simulations (Fig. 1) only explicitly represent neck cutoffs. For each river reach, we also calculate the average channel width and channel migration rate, using the Riverbank Erosion and Accretion from Landsat database of (*21*). The channel width and migration rate, in turn, are used to calculate τ_w (Eq. 2). We plot the empirical observations of τ_w versus τ_{cut} for each river reach and find that the observations are consistent with the scaling produced by our numerical simulations of river meandering (see the Supplementary Materials).

Applying the scaling laws to estimate the storage time distributions of other rivers

In the Supplementary Materials, we provide a step-by-step guide on how to estimate the floodplain age and storage time distributions for any meandering river of interest. The methodology requires the specification of the channel width (W), average migration rate (M_{avg}), and total floodplain width (W_f). The step-by-step guide also explains how to handle multithreaded rivers.

Supplementary Materials

This PDF file includes:

Supplementary Text
Figs. S1 to S22
Tables S1 to S14
References

REFERENCES AND NOTES

1. M. Repasch, J. S. Scheingross, N. Hovius, M. Lupker, H. Wittmann, N. Haghipour, D. R. Gröcke, O. Orfeo, T. I. Eglinton, D. Sachse, Fluvial organic carbon cycling regulated by sediment transit time and mineral protection. *Nat. Geosci.* **14**, 842–848 (2021).
2. M. Dellinger, R. G. Hilton, J. J. Baronas, M. A. Torres, E. I. Burt, K. E. Clark, V. Galy, A. J. Ccahuana Quispe, A. J. West, High rates of rock organic carbon oxidation sustained as Andean sediment transits the Amazon foreland-floodplain. *Proc. Natl. Acad. Sci. U.S.A.* **120**, e2306343120 (2023).
3. J. S. Scheingross, M. N. Repasch, N. Hovius, D. Sachse, M. Lupker, M. Fuchs, I. Halevy, D. R. Gröcke, N. Y. Golombek, N. Haghipour, T. Eglinton, O. Orfeo, A. M. Schleicher, The fate of fluvially-deposited organic carbon during transient floodplain storage. *Earth Planet. Sci. Lett.* **561**, 116822 (2021).
4. M. A. Torres, A. B. Limaye, V. Ganti, M. P. Lamb, A. J. West, W. W. Fischer, Model predictions of long-lived storage of organic carbon in river deposits. *Earth Surf. Dyn.* **5**, 711–730 (2017).
5. M. J. Johnsson, R. H. Meade, Chemical weathering of fluvial sediments during alluvial storage; the Macuapanim Island point bar, Solimoes River, Brazil. *J. Sediment. Res.* **60**, 827–842 (1990).
6. M. Lupker, C. France-Lanord, V. Galy, J. Lavé, J. Gaillardet, A. P. Gajurel, C. Guilmette, M. Rahman, S. K. Singh, R. Sinha, Predominant floodplain over mountain weathering of Himalayan sediments (Ganga basin). *Geochim. Cosmochim. Acta* **84**, 410–432 (2012).
7. J. Bouchez, J. Gaillardet, M. Lupker, P. Louvat, C. France-Lanord, L. Maurice, E. Armijos, J.-S. Moquet, Floodplains of large rivers: Weathering reactors or simple silos? *Chem. Geol.* **332**, 166–184 (2012).
8. M. J. Bickle, H. J. Chapman, E. Tipper, A. Galy, L. Christina, T. Ahmad, Chemical weathering outputs from the flood plain of the Ganga. *Geochim. Cosmochim. Acta* **225**, 146–175 (2018).
9. R. G. Hilton, A. J. West, Mountains, erosion and the carbon cycle. *Nat. Rev. Earth Environ.* **1**, 284–299 (2020).
10. D. Walling, P. Owens, J. Carter, G. Leeks, S. Lewis, A. Meharg, J. Wright, Storage of sediment-associated nutrients and contaminants in river channel and floodplain systems. *Appl. Geochem.* **18**, 195–220 (2003).
11. M. G. Macklin, P. A. Brewer, K. A. Hudson-Edwards, G. Bird, T. J. Coulthard, I. A. Dennis, P. J. Lechler, J. R. Miller, J. N. Turner, A geomorphological approach to the management of rivers contaminated by metal mining. *Geomorphology* **79**, 423–447 (2006).
12. R. Aalto, J. W. Lauer, W. E. Dietrich, Spatial and temporal dynamics of sediment accumulation and exchange along Strickland River floodplains (Papua New Guinea) over decadal-to-centennial timescales. *J. Geophys. Res. Earth Surf.* **113**, 10.1029/2006JF000627 (2008).
13. M. B. Singer, R. Aalto, L. A. James, N. E. Kilham, J. L. Higson, S. Ghoshal, Enduring legacy of a toxic fan via episodic redistribution of California gold mining debris. *Proc. Natl. Acad. Sci. U.S.A.* **110**, 18436–18441 (2013).
14. B. Z. Foreman, K. M. Straub, Autogenic geomorphic processes determine the resolution and fidelity of terrestrial paleoclimate records. *Sci. Adv.* **3**, e1700683 (2017).
15. K. M. Straub, R. A. Duller, B. Z. Foreman, E. A. Hajek, Buffered, incomplete, and shredded: The challenges of reading an imperfect stratigraphic record. *J. Geophys. Res. Earth Surf.* **125**, e2019JF005079 (2020).
16. D. J. Jerolmack, C. Paola, Shredding of environmental signals by sediment transport. *Geophys. Res. Lett.* **37**, 10.1029/2010GL044638 (2010).
17. D. N. Bradley, G. E. Tucker, The storage time, age, and erosion hazard of laterally accreted sediment on the floodplain of a simulated meandering river. *J. Geophys. Res. Earth Surf.* **118**, 1308–1319 (2013).
18. J. Schwenk, S. Lanzoni, E. Foufoula-Georgiou, The life of a meander bend: Connecting shape and dynamics via analysis of a numerical model. *J. Geophys. Res. Earth Surf.* **120**, 690–710 (2015).
19. J. M. Turowski, F. McNab, A. Bufe, S. Tofelde, Width evolution of channel belts as a random walk. *Earth Surf. Dyn.* **13**, 97–117 (2025).
20. Z. Sylvester, P. Durkin, J. A. Covault, High curvatures drive river meandering. *Geology* **47**, 263–266 (2019).
21. T. Langhorst, T. Pavelsky, Global observations of riverbank erosion and accretion from Landsat imagery. *J. Geophys. Res. Earth Surf.* **128**, e2022JF006774 (2023).
22. J. C. Rowland, J. P. Schwenk, E. Shelef, J. Muss, D. Ahrens, S. Stauffer, A. Pilliouras, B. Crosby, A. Chadwick, M. M. Douglas, P. C. Kemeny, M. P. Lamb, G. K. Li, L. Vulis, Scale-dependent influence of permafrost on riverbank erosion rates. *J. Geophys. Res. Earth Surf.* **128**, e2023JF007101 (2023).
23. A. Ielpi, M. G. Lapôtre, A tenfold slowdown in river meander migration driven by plant life. *Nat. Geosci.* **13**, 82–86 (2020).
24. Z. Sylvester, P. Durkin, S. Hubbard, D. Mohrig, Autogenic translation and counter point bar deposition in meandering rivers. *GSA Bull.* **133**, 2439–2456 (2021).
25. G. H. Allen, T. M. Pavelsky, Global extent of rivers and streams. *Science* **361**, 585–588 (2018).
26. E. Greenberg, A. J. Chadwick, V. Ganti, A generalized area-based framework to quantify river mobility from remotely sensed imagery. *J. Geophys. Res. Earth Surf.* **128**, e2023JF007189 (2023).
27. E. C. Geyman, M. M. Douglas, J.-P. Avouac, M. P. Lamb, Permafrost slows Arctic riverbank erosion. *Nature* **634**, 359–365 (2024).
28. F. Nakamura, S. I. Kikuchi, Some methodological developments in the analysis of sediment transport processes using age distribution of floodplain deposits. *Geomorphology* **16**, 139–145 (1996).
29. A. D. Howard, T. R. Knutson, Sufficient conditions for river meandering: A simulation approach. *Water Resour. Res.* **20**, 1659–1667 (1984).

30. M. M. Douglas, G. K. Li, A. J. West, Y. Ke, J. C. Rowland, J. Schwenk, P. C. Kemeny, A. Piliouras, W. W. Fischer, M. P. Lamb, Permafrost formation in a meandering river floodplain. *AGU Adv.* **5**, e2024AV001175 (2024).
31. H. N. Fisk, *Geological investigation of the alluvial valley of the lower Mississippi River* (War Department, Corps of Engineers, 1944).
32. E. Geyman, Y. Ke, M. Douglas, J. Anadu, K. Dunne, J. Magyar, J. Nghiem, J. Reahl, E. Seelen, I. Smith, V. Soldano, W. Fischer, J. West, M. Lamb, *Floodplain Terrain Age at Three Sites in the Yukon River Watershed: Huslia, Alakanuk, and Beaver (Alaska)* (Arctic Data Center, 2024).
33. B. Schoene, M. P. Eddy, K. M. Samperton, C. B. Keller, G. Keller, T. Adatte, S. F. Khadri, U-Pb constraints on pulsed eruption of the Deccan Traps across the end-Cretaceous mass extinction. *Science* **363**, 862–866 (2019).
34. J. de Leeuw, M. P. Lamb, G. Parker, A. J. Moodie, D. Haught, J. G. Venditti, J. A. Nittrouer, Entrainment and suspension of sand and gravel. *Earth Surf. Dyn.* **8**, 485–504 (2020).
35. C. B. Phillips, C. C. Masteller, L. J. Slater, K. B. Dunne, S. Francalanci, S. Lanzoni, D. J. Merritts, E. Lajeunesse, D. J. Jerolmack, Threshold constraints on the size, shape and stability of alluvial rivers. *Nat. Rev. Earth Environ.* **3**, 406–419 (2022).
36. M. P. Lamb, J. de Leeuw, W. W. Fischer, A. J. Moodie, J. G. Venditti, J. A. Nittrouer, D. Haught, G. Parker, Mud in rivers transported as flocculated and suspended bed material. *Nat. Geosci.* **13**, 566–570 (2020).
37. J. Mason, D. Mohrig, Differential bank migration and the maintenance of channel width in meandering river bends. *Geology* **47**, 1136–1140 (2019).
38. H. Martin, D. Edmonds, Q. Lewis, Four years of meander-bend evolution captured by drone-based lidar reveals lack of width maintenance on the White River, Indiana, USA. *J. Geophys. Res. Earth Surf.* **129**, e2023JF007574 (2024).
39. J. A. Constantine, T. Dunne, J. Ahmed, C. Legleiter, E. D. Lazarus, Sediment supply as a driver of river meandering and floodplain evolution in the Amazon basin. *Nat. Geosci.* **7**, 899–903 (2014).
40. M. Donovan, P. Belmont, Z. Sylvester, Evaluating the relationship between meander-bend curvature, sediment supply, and migration rates. *J. Geophys. Res. Earth Surf.* **126**, e2020JF006058 (2021).
41. E. Greenberg, V. Ganti, The pace of global river meandering influenced by fluvial sediment supply. *Earth Planet. Sci. Lett.* **634**, 118674 (2024).
42. A. B. Limaye, M. P. Lamb, Numerical simulations of bedrock valley evolution by meandering rivers with variable bank material. *J. Geophys. Res. Earth Surf.* **119**, 927–950 (2014).
43. A. Ielpi, D. Viero, M. Lapôtre, A. Graham, M. Ghinassi, A. Finotello, How is time distributed in a river meander belt? *Geophys. Res. Lett.* **50**, e2022GL101285 (2023).
44. E. Geyman, J.-P. Avouac, M. Douglas, K. Dunne, Y. Ke, J. Magyar, J. Reahl, E. Seelen, I. Smith, J. West, M. Lamb, *Quantifying River Migration Rates in the Yukon River Watershed from Optical Satellite Imagery* (Arctic Data Center, 2024).
45. E. Caballero, K. Gupta, I. Rish, D. Krueger, Broken neural scaling laws. arXiv:2210.14891 [cs.LG] (2023).
46. J. C. Brice, Stream channel stability assessment (Tech. Rep. United States Federal Highway Administration, 1982).
47. J. M. Hooke, Magnitude and distribution of rates of river bank erosion. *Earth Surf. Processes* **5**, 143–157 (1980).
48. W. L. Dam, S. Campbell, R. H. Johnson, B. B. Looney, M. E. Denham, C. A. Eddy-Dilek, S. J. Babits, Refining the site conceptual model at a former uranium mill site in Riverton, Wyoming, USA. *Environ. Earth Sci.* **74**, 7255–7265 (2015).
49. P. L. Heller, C. Paola, Downstream changes in alluvial architecture; an exploration of controls on channel-stacking patterns. *J. Sediment. Res.* **66**, 297–306 (1996).
50. J. M. Valenza, D. A. Edmonds, H. K. Martin, C. Sifuentes, S. Toby, Stratigraphic architecture of fluvial fans shaped by downstream changes in avulsion style. *Sedimentology* **71**, 2335–2357 (2024).
51. A. Ielpi, M. G. Lapôtre, M. R. Gibling, C. K. Boyce, The impact of vegetation on meandering rivers. *Nat. Rev. Earth Environ.* **3**, 165–178 (2022).
52. A. Bufe, J. M. Turowski, D. W. Burbank, C. Paola, A. D. Wickert, S. Tofelde, Controls on the lateral channel-migration rate of braided channel systems in coarse non-cohesive sediment. *Earth Surf. Process. Landf.* **44**, 2823–2836 (2019).
53. E. A. Barefoot, J. A. Nittrouer, B. Z. Foreman, E. A. Hajek, G. R. Dickens, T. Baisden, L. Toms, Evidence for enhanced fluvial channel mobility and fine sediment export due to precipitation seasonality during the Paleocene-Eocene thermal maximum. *Geology* **50**, 116–120 (2022).
54. E. Ramos, D. Breecker, J. Barnes, F. Li, P. Gingerich, S. Loewy, A. M. Satkosk, A. A. Baczynski, S. L. Wing, N. R. Miller, J. C. Lassiter, Swift weathering response on floodplains during the Paleocene-Eocene Thermal Maximum. *Geophys. Res. Lett.* **49**, e2021GL097436 (2022).
55. B. Z. Foreman, P. L. Heller, M. T. Clementz, Fluvial response to abrupt global warming at the Palaeocene/Eocene boundary. *Nature* **491**, 92–95 (2012).
56. W. J. McMahon, N. S. Davies, Evolution of alluvial mudrock forced by early land plants. *Science* **359**, 1022–1024 (2018).
57. S. S. Zeichner, J. Nghiem, M. P. Lamb, N. Takashima, J. de Leeuw, V. Ganti, W. W. Fischer, Early plant organics increased global terrestrial mud deposition through enhanced flocculation. *Science* **371**, 526–529 (2021).
58. K. B. Dunne, D. J. Jerolmack, What sets river width? *Sci. Adv.* **6**, eabc1505 (2020).
59. M. M. Douglas, K. L. Miller, M. P. Lamb, Mud cohesion governs unvegetated meander migration rates and deposit architecture. *Geol. Soc. Am. Bull.* **137**, 522–540 (2024).
60. J. Rowland, J. Schwenk, D. Ahrens, Global meta-analysis of published river bank erosion and migration rates (Tech. Rep. U.S. Department of Energy, Office of Scientific and Technical Information, 2019).
61. V. Galy, C. France-Lanord, O. Beyssac, P. Faure, H. Kudrass, F. Palhol, Efficient organic carbon burial in the Bengal fan sustained by the Himalayan erosional system. *Nature* **450**, 407–410 (2007).
62. R. G. Hilton, A. Galy, N. Hovius, M.-J. Horng, H. Chen, Efficient transport of fossil organic carbon to the ocean by steep mountain rivers: An orogenic carbon sequestration mechanism. *Geology* **39**, 71–74 (2011).
63. R. Reimer, P. Reimer, CALIBomb—Calibration of post-bomb C-14 data (2024); http://calib.org/CALIBomb/.
64. A. T. Hayden, M. P. Lamb, A. J. Carney, Similar curvature-to-width ratios for channels and channel belts: Implications for paleo-hydraulics of fluvial ridges on Mars. *Geology* **49**, 837–841 (2021).
65. P. J. Reimer, T. A. Brown, R. W. Reimer, Discussion: Reporting and calibration of post-bomb ^{14}C data. *Radiocarbon* **46**, 1299–1304 (2004).
66. P. J. Reimer, W. E. Austin, E. Bard, A. Bayliss, P. G. Blackwell, C. B. Ramsey, M. Butzin, H. Cheng, R. L. Edwards, M. Friedrich, P. Grootes, The IntCal20 Northern Hemisphere radiocarbon age calibration curve (0–55 cal kBP). *Radiocarbon* **62**, 725–757 (2020).
67. S. Kreutzer, C. Schmidt, M. C. Fuchs, M. Dietze, M. Fischer, M. Fuchs, Introducing an R package for luminescence dating analysis. *Ancient TL* **30**, 1–8 (2012).
68. J. A. Durcan, G. E. King, G. A. Duller, DRAC: Dose rate and age calculator for trapped charge dating. *Quat. Geochronol.* **28**, 54–61 (2015).
69. D. Colarossi, G. Duller, H. Roberts, S. Tooth, R. Lyons, Comparison of paired quartz OSL and feldspar post-IR IRSL dose distributions in poorly bleached fluvial sediments from South Africa. *Quat. Geochronol.* **30**, 233–238 (2015).
70. M. Jain, A. Murray, L. Botter-Jensen, Optically stimulated luminescence dating: How significant is incomplete light exposure in fluvial environments? *Quaternaire* **15**, 143–157 (2004).
71. M. Douglas, R. Blankenship, A. Chadwick, K. Dunne, W. Fischer, E. Geyman, Y. Ke, P. Kemeny, G. Li, J. Magyar, E. Mutter, J. Nghiem, A. Piliouras, J. Reahl, J. Rowland, J. Schwenk, E. Seelen, M. I. Smith, A. J. West, M. Lamb, Geomorphic mapping and permafrost occurrence on the Koyukuk River floodplain near Huslia, Alaska, ESS-DIVE dataset (2023).
72. L. Farquharson, K. Bodony, D. Mann, B. Jones, Nogahabara reconnaissance and initial findings, notes from the August 2011 field trip (Department of Geology, University of Alaska Fairbanks: Fairbanks, AK, USA, 2011), p. 16.
73. M. I. Smith, Y. Ke, E. C. Geyman, J. N. Reahl, M. M. Douglas, E. A. Seelen, J. S. Magyar, K. B. Dunne, E. A. Mutter, W. W. Fischer, M. P. Lamb, A. J. West, Mercury stocks in discontinuous permafrost and their mobilization by dynamic erosion and sedimentation in the Yukon River Basin. *Environ. Res. Lett.* **19**, 084041 (2024).
74. M. M. Douglas, K. B. Dunne, M. P. Lamb, Sediment entrainment and slump blocks limit permafrost riverbank erosion. *Geophys. Res. Lett.* **50**, e2023GL102974 (2023).
75. E. Geyman, J. Anadu, K. Cushman, M. Douglas, K. Dunne, W. Fischer, Y. Ke, M. Lamb, J. Magyar, J. Nghiem, J. Reahl, E. Seelen, I. Smith, J. West, *Field and LiDAR-Based Estimates of Above-Ground Biomass in the Yukon River Watershed, Alaska (2023)* (Arctic Data Center, 2024).
76. D. J. Merritts, K. R. Vincent, E. E. Wohl, Long river profiles, tectonism, and eustasy: A guide to interpreting fluvial terraces. *J. Geophys. Res. Solid Earth* **99**, 14031–14050 (1994).
77. N. J. Finnegan, W. E. Dietrich, Episodic bedrock strath terrace formation due to meander migration and cutoff. *Geology* **39**, 143–146 (2011).
78. L. C. Malatesta, J. P. Prancevic, J.-P. Avouac, Autogenic entrenchment patterns and terraces due to coupling with lateral erosion in incising alluvial channels. *J. Geophys. Res. Earth Surf.* **122**, 335–355 (2017).
79. A. B. Limaye, M. P. Lamb, Numerical model predictions of autogenic fluvial terraces and comparison to climate change expectations. *J. Geophys. Res. Earth Surf.* **121**, 512–544 (2016).
80. R. F. Galbraith, R. G. Roberts, G. M. Laslett, H. Yoshida, J. M. Olley, Optical dating of single and multiple grains of quartz from Jinmium rock shelter, northern Australia: Part I, experimental design and statistical models. *Archaeometry* **41**, 339–364 (1999).
81. N. J. Pastick, M. T. Jorgenson, B. K. Wylie, S. J. Nield, K. D. Johnson, A. O. Finley, Distribution of near-surface permafrost in Alaska: Estimates of present and future conditions. *Remote Sens. Environ.* **168**, 301–315 (2015).
82. E. Eriksson, Compartment models and reservoir theory. *Annu. Rev. Ecol. Syst.* **2**, 67–84 (1971).
83. B. Bolin, H. Rodhe, A note on the concepts of age distribution and transit time in natural reservoirs. *Tellus* **25**, 58–62 (2022).

84. W. E. Dietrich, T. Dunne, N. F. Humphrey, L. M. Reid, Construction of sediment budgets for drainage basins, in *Sediment Budgets and Routing in Forested Drainage Basins* (USDA Forest Service, 1982), vol. 141, pp. 5–23.

Acknowledgments: We thank the Huslia, Beaver, and Alakanuk tribal and village councils for river and land access and the Yukon River Inter-Tribal Watershed Council for logistical support. We thank A. Attla, D. Dayton, S. Huffman, K. Vanderpool, R. Williams, C. Wiehl, J. Isidore, P. Phillips Jr., R. Stanislaus, and J. Stronghearts for river navigation and expertise. We thank M. Douglas for creating the initial version of the floodplain relative age map at Huslia (*30*). We also thank J. Anadu, R. Blankenship, M. Douglas, K. Dunne, H. Dion-Kirschner, E. Mutter, J. Nghiem, E. Seelen, and I. Smith for help in the field. **Funding:** This work was supported by NSF award 2127442 and Caltech's Resnick Sustainability Institute. E.C.G. thanks the NSF Graduate Research Fellowships Program and the Fannie and John Hertz Foundation. **Author contributions:** Conceptualization: E.C.G., M.P.L., W.W.F., and A.J.W. Methodology: E.C.G. and M.P.L. Investigation: E.C.G., Y.K., J.S.M., J.N.R., V.S., N.D.B., A.J.W., W.W.F., and M.P.L. Visualization: E.C.G. Supervision: A.J.W., W.W.F., and M.P.L. Writing—original draft: E.C.G. and M.P.L. Writing—review and editing: E.C.G., Y.K., J.S.M., J.N.R., V.S., N.D.B., A.J.W., W.W.F., and M.P.L. **Competing interests:** The authors declare that they have no competing interests. **Data and materials availability:** All data needed to evaluate the conclusions in the paper are present in the paper and/or the Supplementary Materials. The ^{14}C data, OSL data, and relative age maps are archived at https://doi.org/10.18739/A2NC5SF1K. The satellite-derived migration rates, based on the algorithm of Geyman *et al.* (*27*), are archived at https://doi.org/10.18739/A2WW7719J.

Submitted 24 November 2024
Accepted 7 March 2025
Published 11 April 2025
10.1126/sciadv.adu8574

Science Advances

Scaling laws for sediment storage and turnover in river floodplains

Emily C. Geyman, Yutian Ke, John S. Magyar, Jocelyn N. Reahl, Vincent Soldano, Nathan D. Brown, A. Joshua West, Woodward W. Fischer, and Michael P. Lamb

Sci. Adv. **11** (15), eadu8574. DOI: 10.1126/sciadv.adu8574